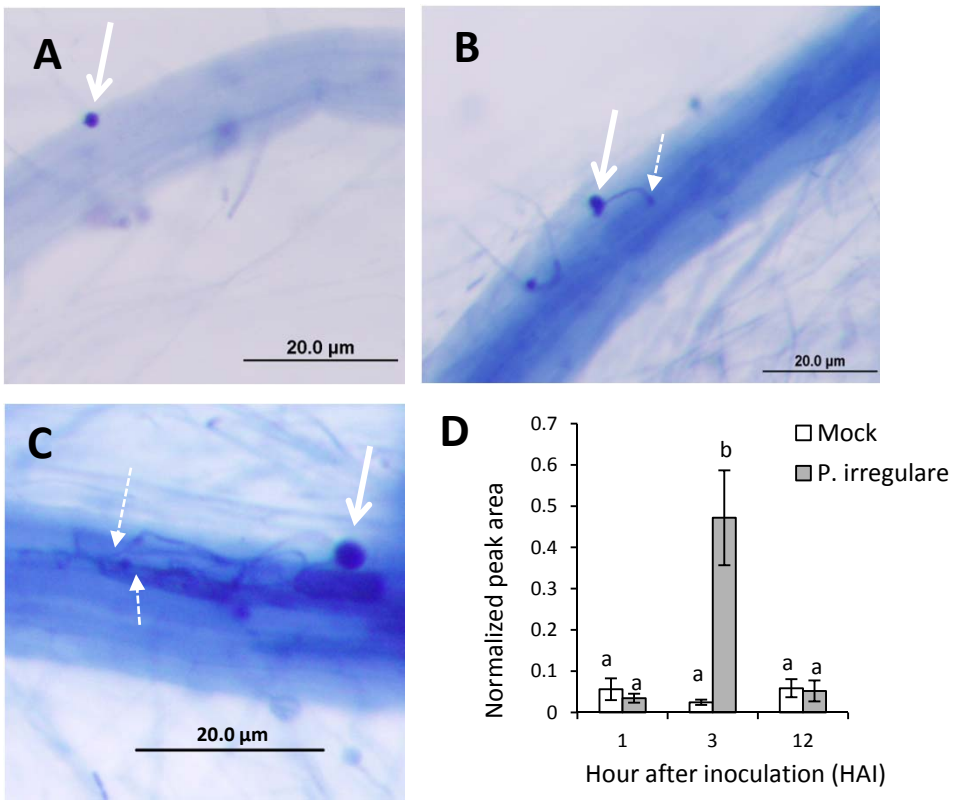

Supplemental Figure 1. Infection of *Arabidopsis* roots with *P. irregulare* and DMNT emission.

Five-day-old *Arabidopsis* seedlings were used to monitor the infection process. A uniform suspension of mycelium and oospores of a one week-old *P. irregulare* culture grown on potato dextrose agar plates was used for infection. Seedlings were observed after staining with lactophenol-tryphan blue. **(A)** *Pythium* oospore (solid arrow) attached to the root surface 1 h post inoculation. **(B)** Oospore (solid arrow) with infection hyphae and appresorium (dashed arrow) and **(C)** penetration of root epidermal cells by infection hyphae (dashed arrows) 3 h post inoculation. **(D)** DMNT emission from axenically grown roots at 1 h, 3 h, and 12 h post inoculation. Normalized peak areas are shown. Values represent the mean ± SE of three biological replicates. Different letters show significant differences based on two-way ANOVA, and Tukey-Kramer HSD test (P=0.0051).

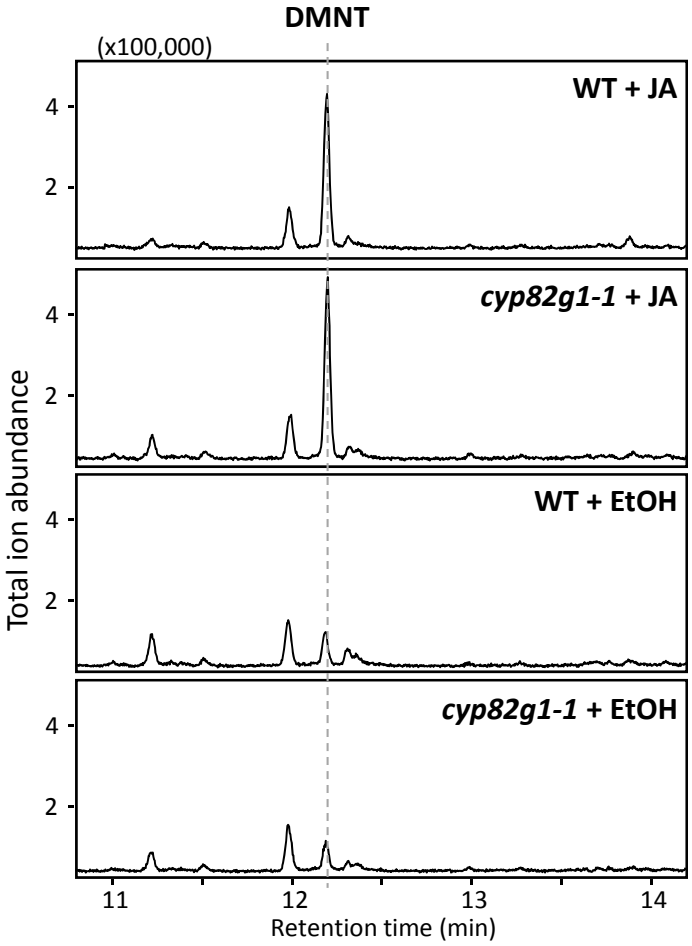

Supplemental Figure 2. The *cyp82g1-1* T-DNA insertion mutant is not impaired in JA -induced production of DMNT in roots.

GC/MS chromatograms of DMNT emission in roots of the *cyp82g1-1* mutant and wild type Col-0 plants upon treatment with JA or ethanol as a control. DMNT emission is not impaired in the *cyp82g1-1* mutant suggesting a role for other cytochrome P450 enzymes in root-specific DMNT formation.

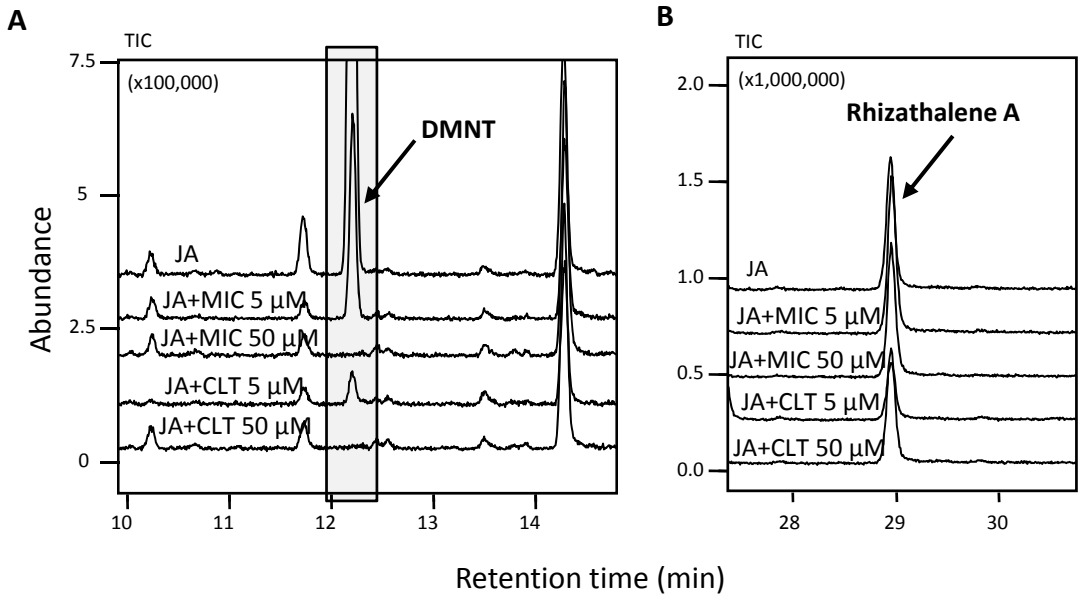

Supplemental Figure 3. Pharmacological study of DMNT formation in *Arabidopsis* hairy root culture.

(A) Treatment of hairy roots with the cytochrome P450 monooxygenase-specific azole inhibitors miconazole (MIC) and clotrimazole (CLT) at 50 µM concentration resulted in abolishing the jasmonate (JA)-induced production of DMNT. **(B)** Production of the recently characterized volatile diterpene rhizathalene (Vaughan et al., 2013) was not affected by inhibitor treatment.

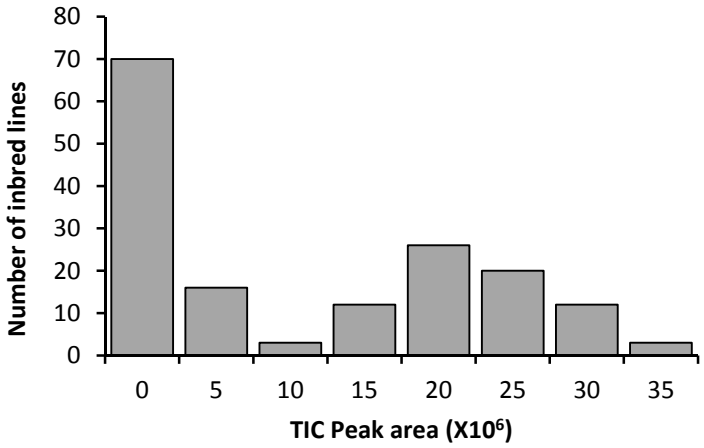

Supplemental Figure 4. Frequency distribution of DMNT emission levels from JA-treated Cvi X Ler recombinant inbred lines.

The DMNT emission level frequencies upon JA treatment in 162 RILs represent a bimodal distribution in the population. The X axis is showing DMNT emission frequency groups for total ion chromatograms (TIC) from a single measurement for each RIL. The Y axis is showing the total number of RILs in each frequency group. A total of 43% of RILs did not emit detectable levels of DMNT while 57% were positive for the presence of DMNT in the root headspace.

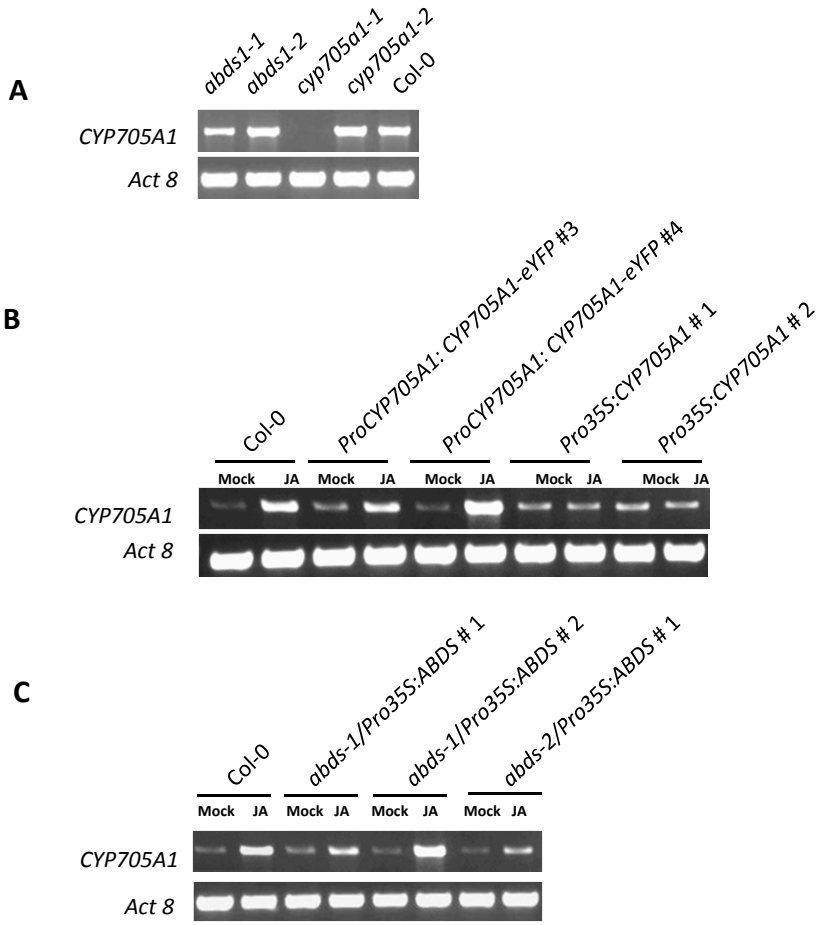

Supplemental Figure 5. RT-PCR analysis of *CYP705A1* transcript levels in *cyp705a1* and *abds* mutants and in *CYP705A1* and *ABDS* transgenic lines.

RT-PCR analysis was performed on mRNA extracted from roots treated with 100 µM JA or mock for 24 h. The full length *CYP705A1* gene was amplified from cDNA prepared from different lines. An internal transcript of *Actin 8* was used as a control. **(A)** *CYP705A1* transcript abundance in JA-treated roots of wild type Col-0, two *cyp705a1* and two *abds* T-DNA insertion lines. **(B)** *CYP705A1* gene expression in roots of wild type Col-0 plants and transgenic lines expressing *CYP705A1* under the control of the native promoter fused to eYFP or the *CaMV 35S* promoter in the background of the *cyp705a1-1* mutant. **(C)** *CYP705A1* gene expression in roots of wild type Col-0 plants and transgenic lines expressing *ABDS* under the control of the *CaMV 35S* promoter in the background of the *abds-1 and abds-2* mutants.

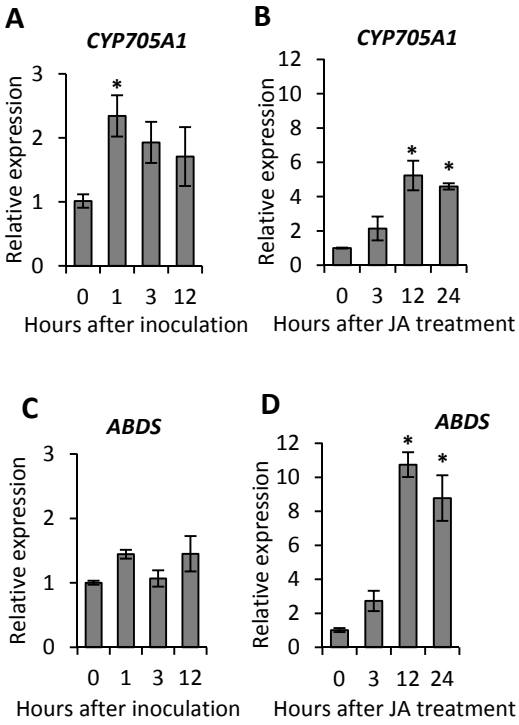

Supplemental Figure 6. qRT-PCR analysis of *CYP705A1* and *ABDS* transcript levels.

Relative transcript levels of *CYP705A1* and *ABDS* were determined in Col-0 plants inoculated with *Pythium* **(A and C)** or treated with 100 µM JA **(B and D)** over a series of several time points. Values were normalized to those of *UBC21* and represent means ± SE of three biological replicates. Transcript levels at 0 h time point were arbitrary set to 1. Asterisks indicate statistically significant differences among means compared to transcript levels at 0 h time point calculated by one-way ANOVA and student *t*-test ($P < 0.005$). No significant difference was found in *ABDS* transcript levels upon inoculation with *Pythium*.

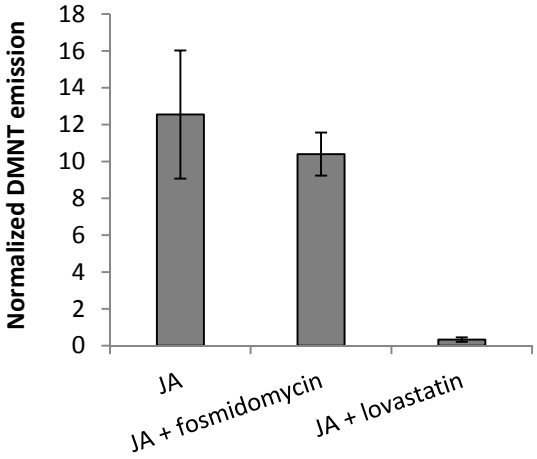

Supplemental Figure 7. DMNT formation in *Arabidopsis* roots is dependent on the mevalonate pathway for precursor biosynthesis.

JA-induced DMNT formation in *Arabidopsis* hairy roots was not effected by fosmidomycin treatment at 400 µM. Volatile DMNT emission was severely reduced in response to treatment with the mevalonate pathway inhibitor lovastatin at 50 µM suggesting a mevalonate dependent terpene biosynthetic route. Error bars represent SD ± mean values of three replicates. JA was applied at 100 µM for 24 h.

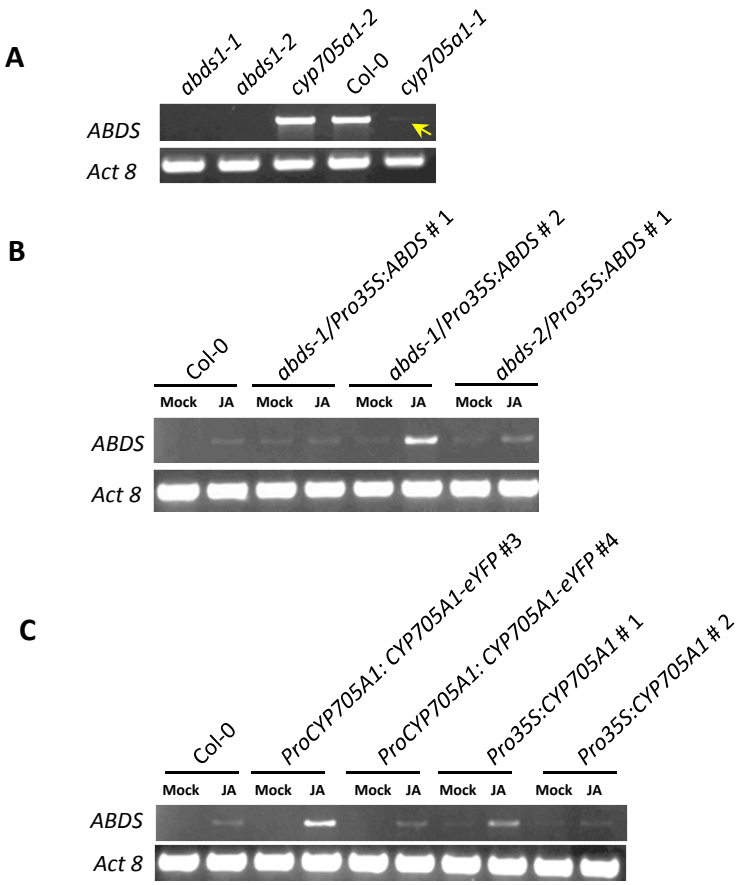

Supplemental Figure 8. RT-PCR analysis of *ABDS* transcript levels in *cyp705a1* and *abds* mutants and in *CYP705A1* and *ABDS* transgenic lines.

RT-PCR analysis was performed on mRNA extracted from roots treated with 100 µM JA or mock for 24 h. The full length *ABDS* gene was amplified from cDNA prepared from different lines. An internal transcript of *Actin 8* was used as a control. **(A)** *ABDS* transcript abundance in JA-treated roots of wild type Col-0, two *cyp705a1* and two *abds* T-DNA insertion lines. The arrow marks a weak *ABDS* amplicon in the *cyp705a1-1* mutant background. Low levels of the *ABDS* transcript in the absence of a functional *CYP705A1* gene indicate a possible feed-back regulatory mechanism. **(B)** *ABDS* gene expression in roots of wild type Col-0 plants and transgenic lines expressing *ABDS* under the control of the *CaMV 35S* promoter in the background of the *abds-1 and abds-2* mutants. **(C)** *CYP705A1* gene expression in roots of wild type Col-0 plants and transgenic lines expressing *CYP705A1* under the control of the native promoter fused to eYFP or the *CaMV 35S* promoter in the background of the *cyp705a1-1* mutant.

A

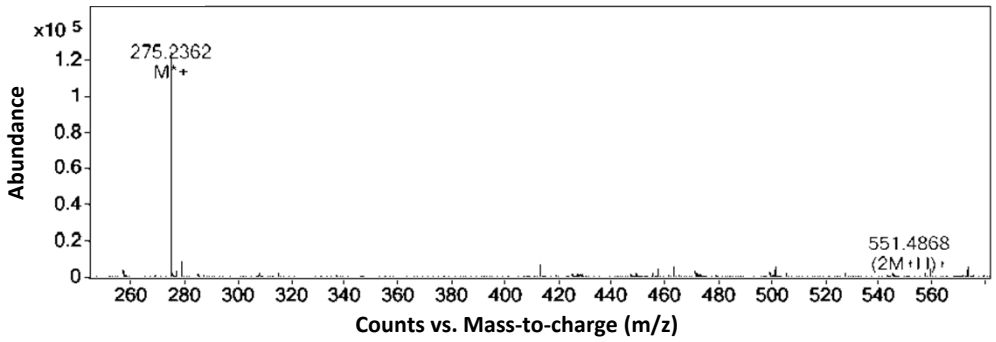

B

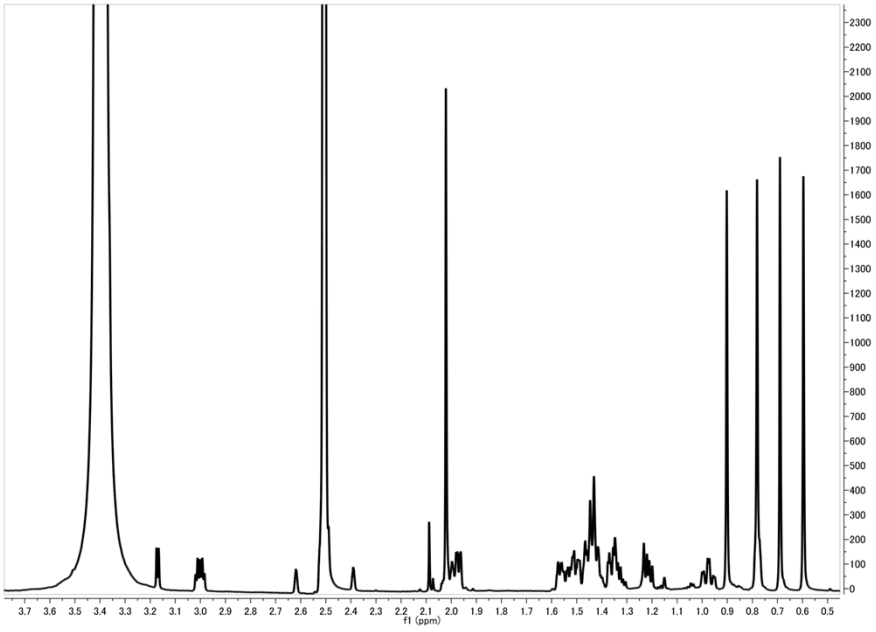

Supplemental Figure 9. HRESIMS analysis and ^{1}H-NMR spectrum of 14-apo-arabidiol.

(A) Detection of the pseudomolecular ion peak at *m/z* 275.2362, $[M\text{-}OH]^{+}$. The *m/z* 551.4868 ion is for $(2M+H)^{+}$ or $C_{38}H_{63}O_2$ calculated for 551.4823. **(B)** Full ^{1}H-NMR spectrum of 14-apo-arabidiol.

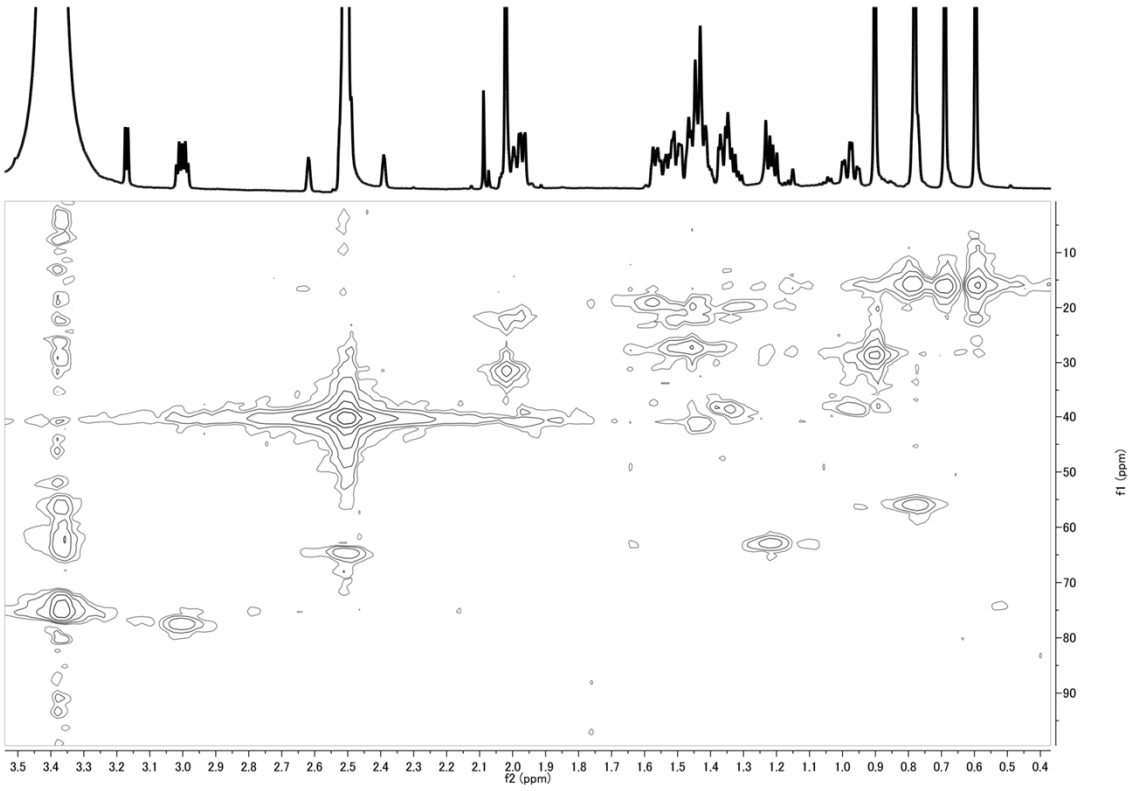

Supplemental Figure 10. HSQC NMR spectrum of 14-apo-arabidiol.

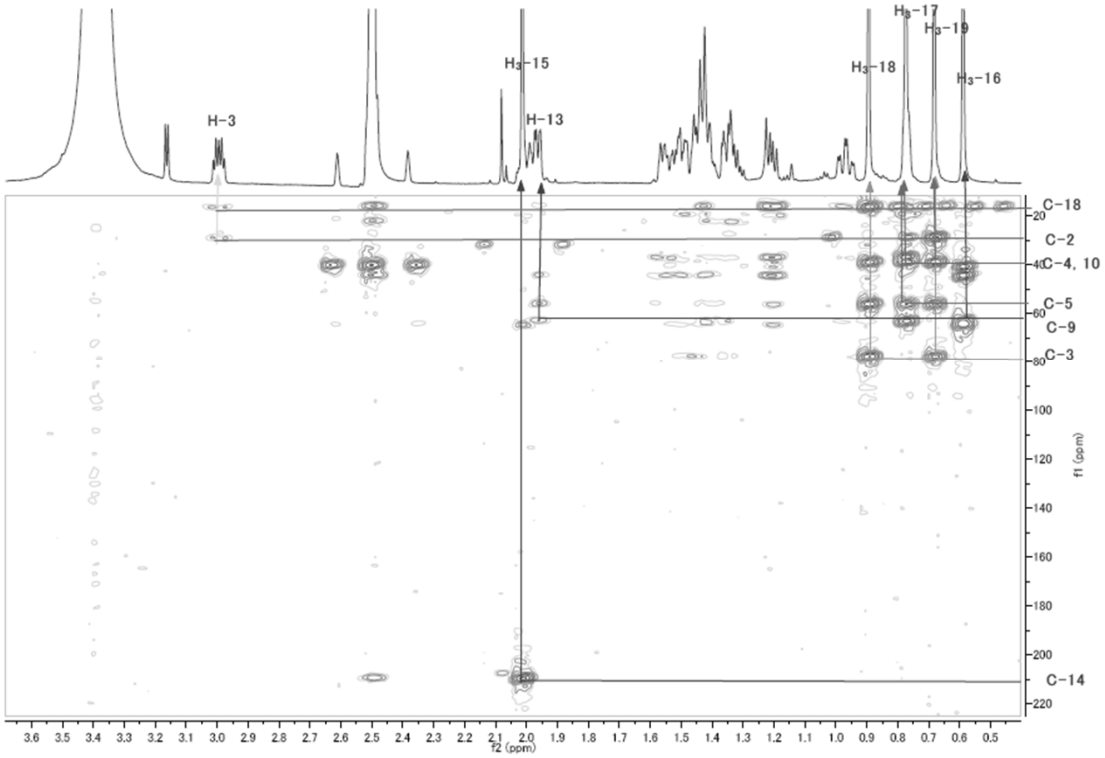

Supplemental Figure 11. Full HMBC NMR spectrum of 14-apo-arabidiol.

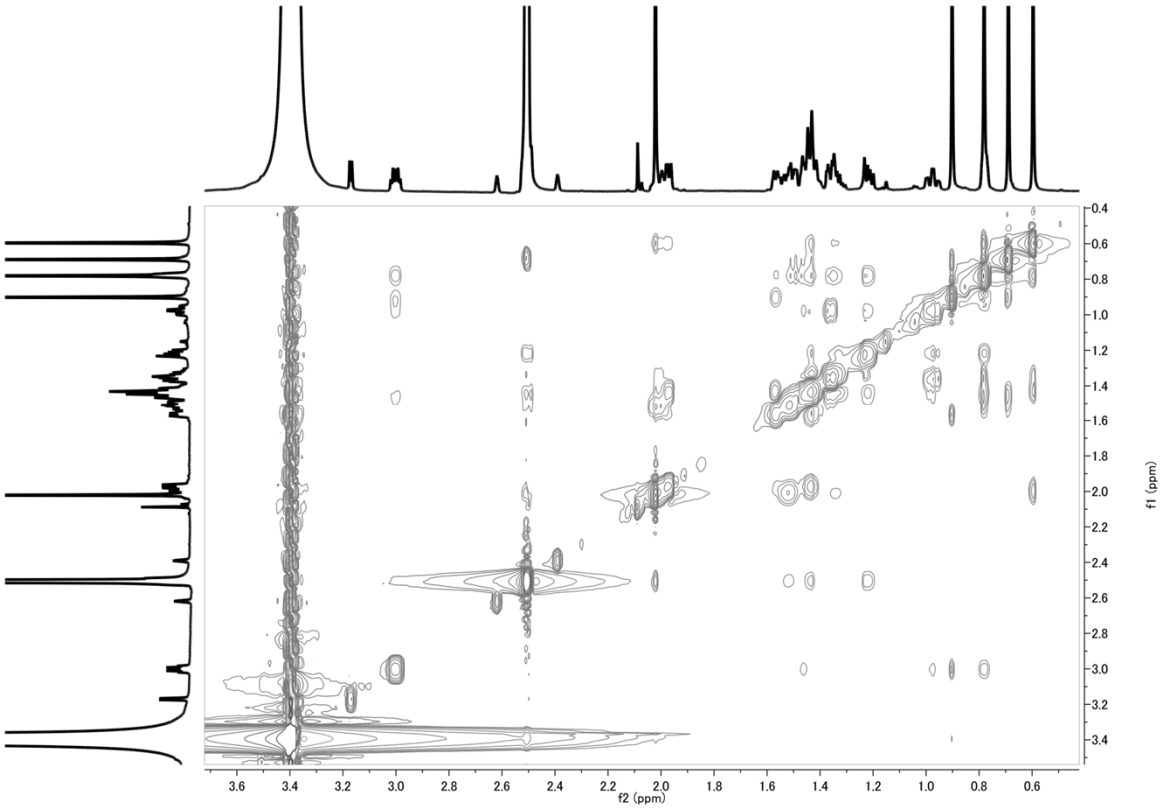

Supplemental Figure 12. NOESY NMR spectrum of 14-apo-arabidiol.

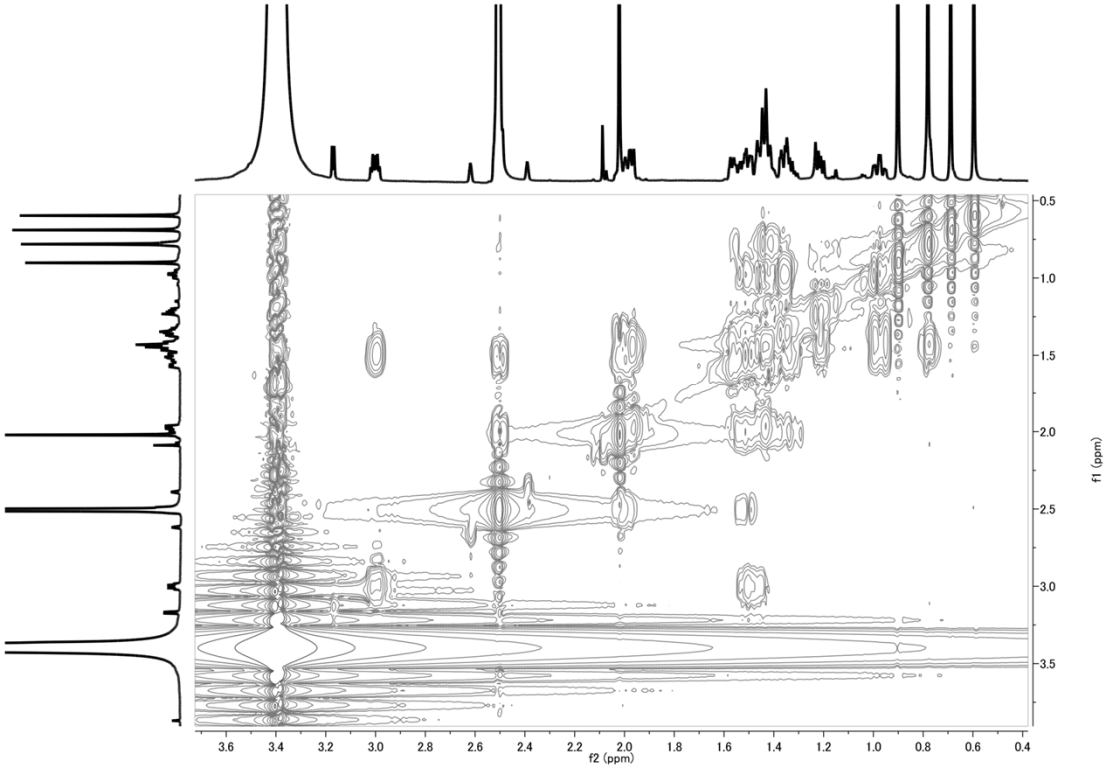

Supplemental Figure 13. COSY NMR spectrum of 14-apo-arabidiol.

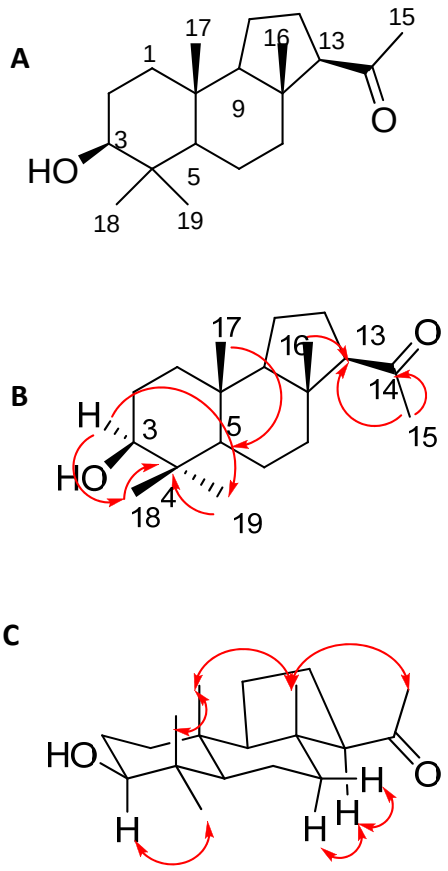

Supplemental Figure 14. Structure of 14-apo-arabidiol.

(A) Structure of 14-apo-arabidiol with atom numbering.
(B) Key HMBC correlations observed in 14-apo-arabidiol.
(C) Key NOE correlations observed in 14-apo-arabidiol.

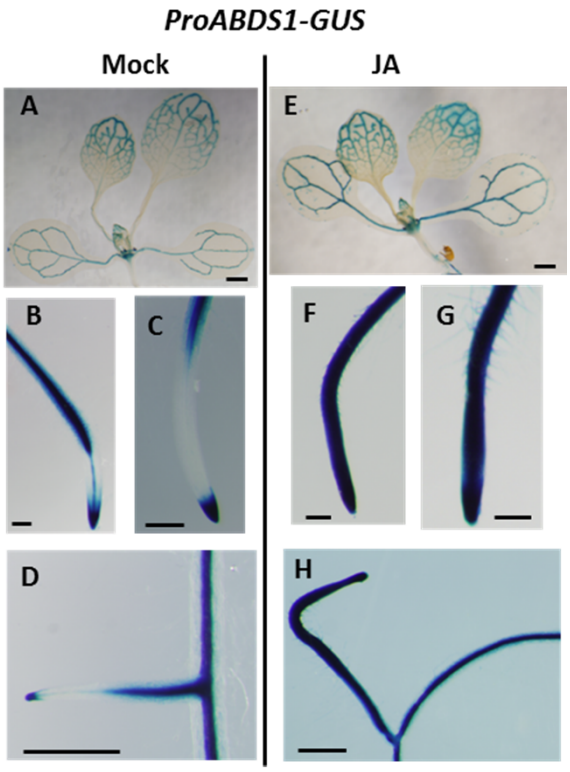

Supplemental Figure 15. *ABDS* promoter-*GUS* gene expression patterns.

GUS activity in twelve-day-old mock and JA-treated *ProABDS-GUS* transgenic lines. **(A, E)** Cotyledon and true leaves; Bar = 1 mm; **(B, F)** Main root tip; Bar = 200 µm; **(C, G)** Lateral root tip; Bar = 200 µm; **(D, H)** Lateral –main root attachment site; Bar = 0.5 mm.

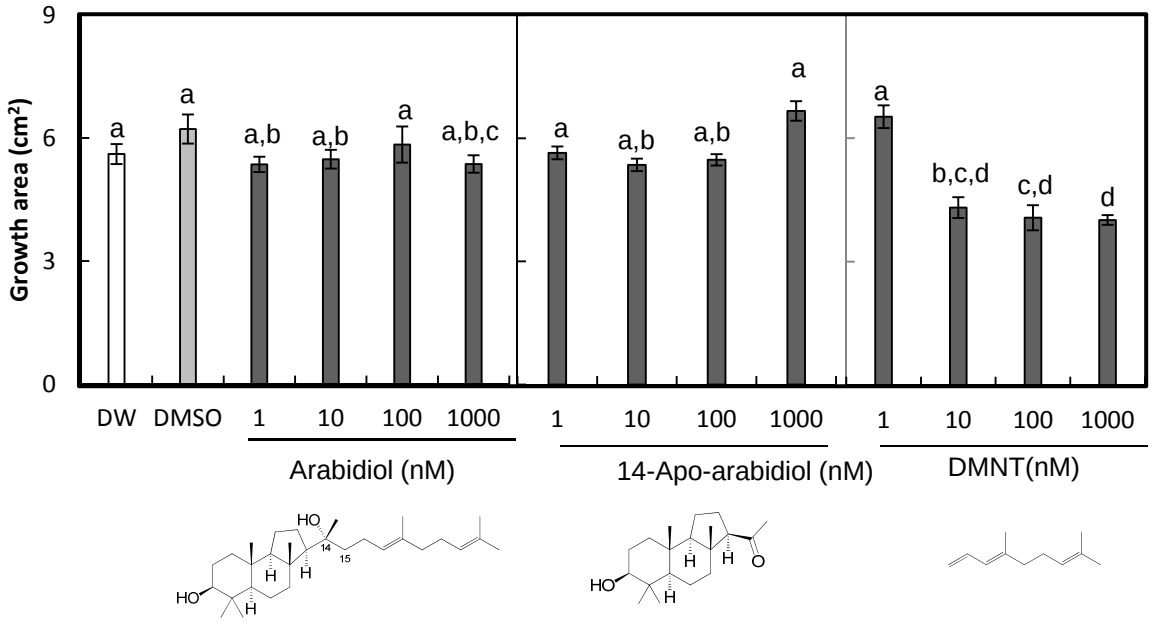

Supplemental Figure 16. Effect of arabidiol, 14-apo-arabidiol, and DMNT on the growth of *P. irregulare* 110305.

Different amounts of chemicals were applied to 10 mL of fresh potato dextrose agar plates. An agar plug with *Pythium* mycelium (2X2 mm) was positioned in the center of each plate and incubated at room temperature under dark condition. The *Pythium* growth zone was determined 2 days after inoculation. Data represent the mean value ± standard error mean of at least four replicates. Different letters show significant differences based on one-way ANOVA, Tukey-Kramer HSD test; $P<0.001$.

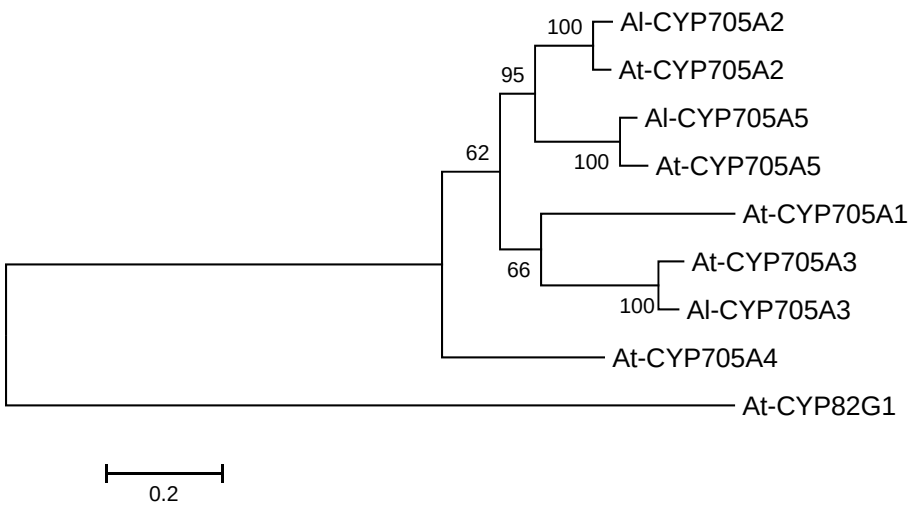

Supplemental Figure 17. Molecular phylogenetic analysis of *A. thaliana* and *A. lyrata* CYP705 members of the *ABDS* and *THAS* gene clusters.

A maximum likelihood tree is presented for 8 selected members of CYP705A from *A. thaliana* and *A. lyrata*. The TMTT/DMNT synthase CYP82G1 from *A. thaliana* was used as an outgroup since it is a member of the CYP71 clan and catalyzes a similar biochemical reaction. Evolutionary analyses were conducted in MEGA5 (Tamura et al., 2011). The tree is drawn to scale with branch lengths measured in the number of substitutions per site. Bootstrap values were performed with 1000 replicates. At, *Arabidopsis thaliana*; Al, *Arabidopsis lyrata*.

	L(115)	I(123)	T(213)	F(223)	F(224)	E(303)	F(304)	G(307)	A(308)	A(309)	D(310)	A(311)	P(371)	T(372)	V(375)	V(376)	M(491)	A(492)	%
A1	L	I	V	I	F	D	L	A	G	T	D	T	P	G	L	p	M	A	40
A2	L	L	V	I	F	E	F	G	G	T	D	T	P	S	L	I	M	V	45
A3	L	I	A	L	F	D	L	A	G	T	E	N	P	G	F	L	M	A	40
A4	L	I	V	H	F	D	L	A	G	T	E	A	P	G	V	V	M	A	50
A5			*	*					*	*				*					

Supplemental Figure 18. Sequence alignment of active site residues of CYP705A1 to CYP705A5.

Homology modeling of A2-A5 using the structure of CYP705A1 as the template gives evidence that several alterations in the active site may be associated with the lack of activity toward the oxidative degradation of arabidiol in A2-A5. The letter size at each position is proportional to the degree of amino acid conservation. The residues interacting with arabidiol (any atom in 5 Å including main chain) are listed and aligned to the equivalent residues in other member of this family (A2-A5). These major changes are highlighted with * in the table. The figure is prepared by WebLogo (Crooks, et al., 2004).

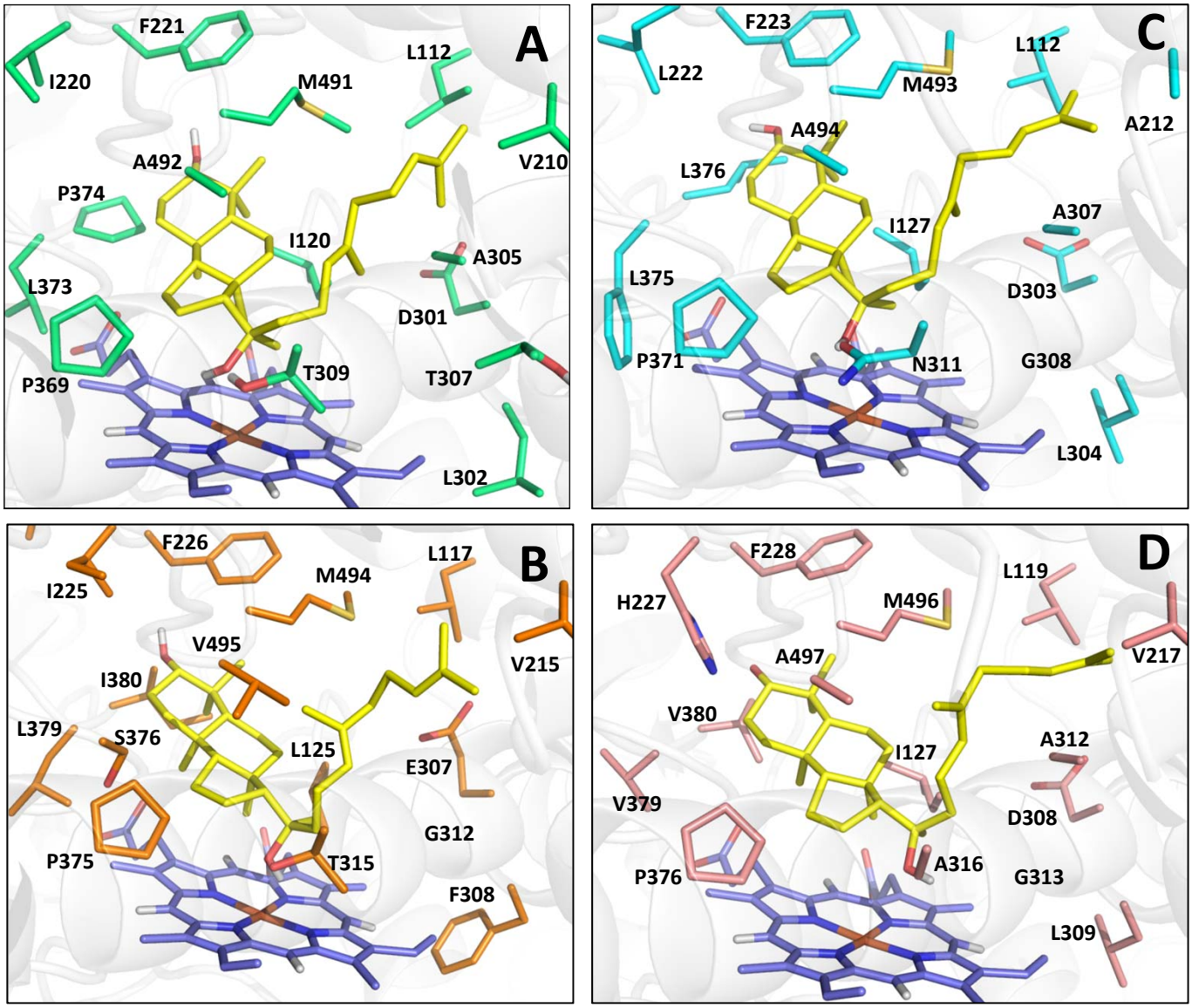

Supplemental Figure 19. Docked conformations of arabidiol into the active sites of CYP705A2-A5.

All structures were generated using a multi-alignment homology modeled CYP705A1 structure as the single template. **(A)** CYP705A2, **(B)** CYP705A3, **(C)** CYP705A4, **(D)** CYP705A5. Using AutoDock-Vina, arabidiol was docked into the active site of each A2 to A5. The most energetically favorable orientation of arabidiol (with binding energy of -8.9, -9.6, -9.2 and -8.8 Kcal/mol for CYP705A2 to CYP705A5 structures, respectively) is shown for each structure. Although the binding energies do not change significantly among A1-A5, arabidiol takes a completely reverse orientation in the active site of A2-A5 in comparison to A1. the difference in orientation can be mainly related to the replacement of Phe223 of A1 with residues of smaller side-chains in structures of A2-A5 (Ile220 of A2, Ile225 of A3, Leu222 of A4 and His227 of A5). This replacement allows the ring containing side of arabidiol to be accommodated into the region of the active site with higher hydrophobic interactions. Furthermore, residue Thr213 in A1 (which makes a H-bond to C3-OH of arabidiol) is also replaced by hydrophobic residues in A2-A5 (Val210 in A2, Val215 in A3, Ala212 in A4 and Val217 in A5) that may disfavor the A1 orientation of arabidiol in the A2-A5 structures.

RIL Name	(*E*)-DMNT Peak area	RIL Name	(*E*)-DMNT Peak area	RIL Name	(*E*)-DMNT Peak area	RIL Name	(*E*)-DMNT Peak area	RIL Name	(*E*)-DMNT Peak area	RIL Name	(*E*)-DMNT Peak area
CS22001	0	CS22030	0	CS22059	25133347	CS22088	0	CS22117	20590112	CS22146	15477159
CS22002	0	CS22031	27058049	CS22060	23740	CS22089	16913460	CS22118	27788861	CS22147	27448273
CS22003	0	CS22032	19351172	CS22061	18842594	CS22090	25678	CS22119	0	CS22148	0
CS22004	0	CS22033	0	CS22062	20465850	CS22091	0	CS22120	12688958	CS22149	0
CS22005	22059934	CS22034	19378957	CS22063	29855640	CS22092	0	CS22121	20817947	CS22150	23626411
CS22006	0	CS22035	0	CS22064	17135526	CS22093	0	CS22122	0	CS22151	0
CS22007	27736749	CS22036	0	CS22065	0	CS22094	13559979	CS22123	0	CS22152	11450557
CS22008	24122014	CS22037	16548314	CS22066	0	CS22095	26481940	CS22124	0	CS22153	1166438
CS22009	0	CS22038	19884702	CS22067	3866463	CS22096	0	CS22125	17719587	CS22154	18701140
CS22010	18701264	CS22039	0	CS22068	0	CS22097	28958243	CS22126	48055	CS22155	0
CS22011	20502662	CS22040	18052038	CS22069	0	CS22098	0	CS22127	0	CS22156	16881894
CS22012	14097389	CS22041	0	CS22070	15143672	CS22099	20707182	CS22128	0	CS22157	31249655
CS22013	13683678	CS22042	15553726	CS22071	18282569	CS22100	0	CS22129	24732086	CS22158	0
CS22014	18115208	CS22043	0	CS22072	66492	CS22101	23579798	CS22130	0	CS22159	0
CS22015	0	CS22044	5237897	CS22073	364332	CS22102	0	CS22131	21423339	CS22160	0
CS22016	0	CS22045	23265242	CS22074	14401392	CS22103	14092490	CS22132	22826534	CS22161	0
CS22017	25837324	CS22046	0	CS22075	13500422	CS22104	21651477	CS22133	0	CS22162	14427232
CS22018	15563084	CS22047	12218269	CS22076	18090614	CS22105	17953288	CS22134	7932553	Cvi-1	0
CS22019	26706356	CS22048	18096163	CS22077	0	CS22106	14338315	CS22135	0	Ler-2	18930442
CS22020	0	CS22049	27086441	CS22078	3445868	CS22107	19832455	CS22136	19609317		
CS22021	0	CS22050	62480	CS22079	4799598	CS22108	0	CS22137	30949701		
CS22022	22583441	CS22051	0	CS22080	31353853	CS22109	0	CS22138	22216949		
CS22023	9336713	CS22052	63670	CS22081	55863	CS22110	0	CS22139	1725688		
CS22024	0	CS22053	0	CS22082	0	CS22111	28635588	CS22140	23591589		
CS22025	22918893	CS22054	0	CS22083	0	CS22112	0	CS22141	0		
CS22026	23539	CS22055	1860976	CS22084	0	CS22113	24093689	CS22142	22910820		
CS22027	0	CS22056	1235521	CS22085	16642335	CS22114	0	CS22143	0		
CS22028	0	CS22057	0	CS22086	0	CS22115	0	CS22144	12605221		
CS22029	17844601	CS22058	0	CS22087	0	CS22116	17138722	CS22145	0		

Supplemental Table 1. DMNT emission levels in Cvi X L*er* recombinant inbred line population and parental lines.
GC/MS total ion chromatogram (TIC) peak areas of DMNT in JA-treated roots of individual lines are presented.

COR	AGI No.	Gene annotation
0.781	At4g15340	pentacyclic triterpene synthase 1 (Arabidiol synthase)
0.65	At4g31100	wall-associated kinase, putative
0.62	At4g22610	Bifunctional inhibitor/lipid-transfer protein/seed storage 2S albumin superfamily protein

Supplemental Table 2. Candidate genes coexpressed with *CYP705A1* evaluated based on the ATTED-II database.
Annotation and correlation coefficients (COR) were adopted from ATTED-II (http://atted.jp/).

	Proton	Carbon
1	0.97 td, (13.3, 3.9) 1.34 m	38.7
2	1.45 m	27.3
3	3.00 dd (11, 5)	77.4
4		38.7
5	0.70 overlapped	55.9
6	1.56 m	19.7
7	1.49 overlapped	40.5
8		44.0
9	1.22 dd (12.8, 7.3)	63.4
10		38.6
11	1.99 m	21.9
12	1.43 overlapped	22.0
13	2.5 overlapped with the solvent signal	64.1
14		209.2
15	2.01 s	31.4
16	0.58 s	15.7
17	0.78 s	15.4
18	0.88 s	16.2
19	0.68 s	15.8

Supplemental Table 3. Proton and carbon chemical shifts for 14-apo-arabidiol and key correlations from NMR spectra.

Primer	Sequence	Experiment
P1	5'-CACCATGGATGCAATCGTCGTTGACTC-3'	*CYP705A1* cDNA amplification
P2	5'-TTAAAGATGGGAAATTAAAGAGTTTTGGG-3'	*CYP705A1* cDNA amplification
P3	5'-CACCATGTGGAGACTAAGAATTGGAGCTAAGG-3'	*ABDS* cDNA amplification
P4	5'-TCAAGGCTGAAGCCGCCGTAG-3'	*ABDS* cDNA amplification
P5	5'-GGGGACAACTTTGTATAGAAAAGTTGTTGAAAAATGC ACGGTCAATTCTACCTTC-3'	Cloning *CYP705A1* promoter with attB4 (forward)
P6	5'-GGGGACTGCTTTTTTGTACAAACTTGTTGTTGCTGAAAA GCAAAGAAGAGGC-3'	Cloning *CYP705A1* promoter with attB1 (reverse)
P7	5'-CTATGAATTCATGGATGCAATCGTCGTTGACTC-3'	*CYP705A1* forward with *EcoR*I for yeast expression
P8	5'-CTATGAGCTCTTAAAGATGGGAAATTAAAGAGTTTTGGG-3'	*CYP705A1* reverse with *Sac*I for yeast expression
P9	5'-CTATGAGCTCTTAACTTAAGGAAGCTAGAAACCTCTC-3'	mut*CYP705A1* reverse with *Sac*I for yeast expression
P10	5'-TGAGAGGTGGCAGAGATGTG-3'	*CYP71A19*, RT-PCR
P11	5'-ACCAAGTCCGATCTGGTGTC-3'	*CYP71A19*, RT-PCR
P12	5'-AGTAAGGACATTTGCCGCAC-3'	*CYP71A20*, RT-PCR
P13	5'-GACCGGTTGCTTCAGTTAGG-3'	*CYP71A20*, RT-PCR
P14	5'-CTCTCTCAGCCTCGGCTCTC-3'	*CYP81D11*, RT-PCR
P15	5'-TCAACAAATTCGACATCGCC-3'	*CYP81D11*, RT-PCR
P16	5'-ACGGTGATCACTGGCGTAAC-3'	*CYP81D1*, RT-PCR
P17	5'-ATGCCATGTGTGGGACTAGC-3'	*CYP81D1*, RT-PCR
P18	5'-CGAGGAAGAAGGAGAGCGTT-3'	*CYP705A12*, RT-PCR
P19	5'-TGAATCAACCTTTTTCCCCC-3'	*CYP705A12*, RT-PCR
P20	5'-CCAGGGGAGCTTCAATGTTC-3'	*CYP708A3*, RT-PCR
P21	5'-CCAACCAGCCGGAATTGTAT-3'	*CYP708A3*, RT-PCR
P22	5'-CGACGTGAACGTCTCCTCTC-3'	*CYP705A1*, RT-PCR
P23	5'-CCATTGCCCACTGTATTGCT-3'	*CYP705A1*, RT-PCR
P24	5'-CCGCAAGGGATCTCAAGAAG-3'	*CYP71A12*, RT-PCR
P25	5'-ATGAGAGGGAACTTTCGGCA-3'	*CYP71A12*, RT-PCR
P26	5'-TCGTGAACTCGTCACACTCG-3'	*CYP81D8*, RT-PCR
P27	5'-TCTGAAACCAACCGCAAAAC-3'	*CYP81D*8, RT-PCR
P28	5'-GCAGCGAGAGAAAAGAAGCA-3'	*CYP76C4*, RT-PCR
P29	5'-ATACGCTTGGGTCTCGTCCT-3'	*CYP76C4*, RT-PCR
P30	5'-GAGATGAGTAACGCCAAGCG-3'	*CYP78A8*, RT-PCR
P31	5'-ACCAAAACCGCAACAGTGTC-3'	*CYP78A8*, RT-PCR
P32	5'-ACGTACGGACTTGATGGACG-3'	*CYP705A4*, RT-PCR
P33	5'-CCGGGACAACTTCTTCTTCC-3'	*CYP705A4*, RT-PCR
P34	5'-CACTAAGCTGCTCCGACCAC-3'	*CYP705A18*, RT-PCR
P35	5'-TTGGACCGAGGTATCAGTGC-3'	*CYP705A18*, RT-PCR
P36	5'-GGACCTGATGGATGTGCTGT-3'	*CYP705A13*, RT-PCR
P37	5'-TCATGAACTCACGAACTGCG-3'	*CYP705A13*, RT-PCR
P38	5'-AGTTTATGGATGCCTTGTTGGC-3'	*CYP705A1*, qRT-PCR
P39	5'-ATTGCTATTGATGAGGCGTCAG -3'	*CYP705A1*, qRT-PCR
P40	5'-TCTACTTGCAGAGTGATAACGGA-3'	*ABDS*, qRT-PCR
P41	5'-CTCGATGACCGTGTCTTGAACAA-3'	*ABDS*, qRT-PCR
P42	5'-AGTCCTGCTTGGACGCTTCA-3'	*UBC21*, qRT-PCR
P43	5'-GAAGATTCCCTGAGTCGCAGTT-3'	*UBC21*, qRT-PCR

Supplemental Table 4. Sequence of primers used in different experiments.

Supplemental Methods

Growth Inhibition Assay in Vitro

P. irregulare was cultured on half strength potato dextrose agar (Difco213400) containing different concentrations of each chemical. *P. irregulare* plugs taken from water agar were placed in the center of the plate and incubated at room temperature under dark conditions for two days. The growth area was measured and calculated according to Adie et al. (2007) with minor modifications. Hyphal growth from a single inoculate establishes a distinct growth zone, therefore two diameters (R_1, R_2), perpendicular to each other, were measured for each growth zone and the mean was obtained. The growth area was calculated:

$$Area = \pi \left(\frac{R_1 + R_2}{2} \right)^2$$

The growth inhibition assay was repeated at least twice with more than three replicates and the inhibitory effect of chemicals on *Pythium* growth was determined by comparison with the control growth area.

NMR Analysis of 14-Apo-Arabidiol Structure

The ^{1}H NMR spectroscopic data of 14-apo-arabidiol (Supplemental Figure 10B) displayed signals for four quaternary methyl groups (δ 0.58, 0.68, 0.78 and 0.88, each singlet), one singlet (δ 2.01, 3H) corresponding to one methyl group attached to a carbonyl, one oxymethine (δ 3.00, dd, J = 11, 5 Hz) (Supplemental Table 3). The Heteronuclear Single Quantum Coherence (HSQC) (Supplemental Figure 10) coupled with the Heteronuclear Multiple Bond Correlation (HMBC) experiment (Supplemental Figure 11) showed that 14-apo-arabidiol in fact had 19 carbons ascribable to four quaternary carbons including an acetyl carbonyl (δ 209.2, C-14), four methines, one of which attached to an oxygen (δ 77.4, C-3), six methylenes (δ 21.9, 22.0, 29.3, 38.7, 19.7 and 40.5) and five methyls (δ 15.4, 15.7, 15.8, 16.2 and 31.4), (Supplemental Table 3). The four degrees of unsaturation deduced from HRESI mass spectroscopic data and the presence of a carbonyl in the molecule demonstrated that the 14-apo-

arabidiol product must be a tricyclic compound. The allocation of the oxymethine to be at C-3, the acetyl group at C-13 and the presence of a five membered ring (ring C) were substantiated by the interpretation of the HSQC and HMBC spectroscopic data. The long range cross-peaks from the proton at 3.00 ppm (H-3) to the methyl carbon at 16.2 ppm (C-18) and the methylene at C-2 (28.9), from the methyl protons at 0.88 (CH_3-18) to C-3 (77.4 ppm), C-19 (15.8 ppm), C-4 (37.8 ppm) and C-5 (55.9 ppm) allowed us to locate the hydroxyl group at C-3 and two methyl groups at C-4. The attachment of the acetyl group at C-13 was corroborated by long range correlations between the downfielded methyl group (δ 2.01) and both the carbonyl (δ 209.2) and the methine at δ 64.1. The important long range correlations which support the structure of 14-apo-arabidiol are summarized in Supplemental Figure 14B. The relative stereochemistry of 14-apo-arabidiol was deduced by a 2D Nuclear Overhauser Effect SpectroscopY (NOESY) experiment (Supplemental Figure 12). The beta-orientation of the hydroxyl group at C-3 was deduced by the NOE correlations from the proton at 3.00 ppm (H-3) to CH_3-19; from CH_3-18 methyl to CH_3-17 and from CH_3-17 to CH_3-16. Moreover, the alpha-orientation of the proton at C-13 was substantiated by the NOE cross peak between H-13 and the two protons of C-7, and the methyl group at C-14 to CH_3-16 (Supplemental Figure 14C).

Computational Methods

The protein sequence of CYP705A1 (excluding the first 37 residues involve in membrane binding) was blasted against the RCSB Protein Data Bank to search for the optimal template for homology modeling. Three cytochrome P450 conformations were selected based on maximum identity/similarity, high resolution and minimum gap in the structure (PDB: 3RUK_C, 2HI4_A, 4I8V_A) for multiple template comparative modeling using Modeller 9v11 (Marti-Renom et al., 2000). The simulation steps include single template modeling, multiple template modeling, and ab-initio loop refinement (Fiser et al., 2000). Each step includes 1000 independent simulations scored using DOPE (Shen and Sali, 2006) and GA341 (Melo and Sali, 2007) scoring functions. The selected final model was subjected to additional modeling to include the heme group into the protein structure. The loop carrying the cysteine residue bond to the heme group in PDB:3URK has 80% identity to the equivalent loop 439-449 in CYP705A1. The regional alignment of this loop in 3URK and CYP705A1 was used to incorporate the heme into the heme binding site of

CYP705A1. The quality of the final model was verified using PROCHECK (Morris et al., 1992) and Anolea (Melo al., 1997). Due to the high sequence identity (> 65%), the 3D structures of CYP705A2- CYP705A5 from *A. thaliana* were modeled using the structure of CYP705A1 as template.

Molecular dockings were performed using AutoDock-Vina (Trott and Olson, 2010) with exhaustiveness of 10 and evaluation of 10 docked positions in each run. The protonation state of titratable residues in CYP705A1 structure were predicted by H++ (Gordon et al., 2005). The structure of the arabidiol molecule to be docked into the active site of modeled CYP705A1 was taken from the ZINC data base (ZINC 59211647) (Irwin et al., 2012). The ligands were fully flexible during docking and their Gasteiger partial charges (Gasteiger and Marsili, 1980) of ligand and protein were determined by AutoDock Tools 1.5.4 (Morris et al., 1998; Morris et al., 2009). The partial charges distribution over the heme group was calculated as described previously (Lee et al., 2010) using Gaussian09A_02 (Frisch et al., 2009). The main binding cavity of modeled CYP705A1 was determined using AutoLigand (Harris et al., 2008) and via the structural alignment to the templates of comparative modeling. The analysis of the binding cavity shows the side chain of M454 of CYP705A1 (conserved among CYP705A1- CYP705A5) is directly extended into the center of the binding site that fills a major part of the binding cavity. This methionine is replaced by a glycine in all the templates; thus to avoid any biased docking due to the orientation of this Met, another rotamer for Met from the PyMol rotamer library (Dunbrack and Cohen, 1997) was picked for CYP705A1. The most favored docked structure for each compound was selected based on the lowest binding energy using three independent replicated docking experiments.

Supplemental References

Adie, B.A., Perez-Perez, J., Perez-Perez, M.M., Godoy, M., Sanchez-Serrano, J.J., Schmelz, E.A., and Solano, R. (2007). ABA is an essential signal for plant resistance to pathogens affecting JA biosynthesis and the activation of defenses in *Arabidopsis*. Plant Cell **19,** 1665-1681.

Crooks, G.E., Hon, G., Chandonia, J.M., and Brenner, S.E. (2004). WebLogo: a sequence logo generator. Genome Res. **14:** 1188-1190.

Dunbrack, R.L.Jr. and Cohen, F.E. (1997). Bayesian statistical analysis of protein side-chain rotamer preferences. Protein Sci. **6:** 1661–1681.

Fiser, A., Do, R.K.G., and Sali, A. (2000). Modeling of loops in protein structures. Protein Sci. **9:** 1753-1773.

Frisch, M.J., Trucks, G.W., Schlegel, H.B., Scuseria, G.E., Robb, M.A., Cheeseman, J.R., Scalmani, G., Barone, V., Mennucci, B., Petersson, G.A., Nakatsuji, H., Caricato, M., Li, X., Hratchian, H.P., Izmaylov, A.F., Bloino, J., Zheng, G., Sonnenberg, J.L., Hada, M., Ehara, M., Toyota, K., Fukuda, R., Hasegawa, J., Ishida, M., Nakajima, T., Honda, Y., Kitao, O., Nakai, H., Vreven, T., Montgomery, J., J. A. , Peralta, J.E., Ogliaro, F., Bearpark, M., Heyd, J.J., Brothers, E., Kudin, K.N., Staroverov, V.N., Kobayashi, R., Normand, J., Raghavachari, K., Rendell, A., Burant, J.C., Iyengar, S.S., Tomasi, J.C., M.; Rega, N., Millam, N.J., Klene, M., Knox, J.E., Cross, J.B., Bakken, V., Adamo, C., Jaramillo, J., Gomperts, R., Stratmann, R.E., Yazyev, O., Austin, A.J., Cammi, R., Pomelli, C., Ochterski, J.W., Martin, R.L., Morokuma, K., Zakrzewski, V.G., Voth, G.A., Salvador, P., Dannenberg, J.J., Dapprich, S., Daniels, A.D., Farkas, Ö., Foresman, J.B., Ortiz, J.V., Cioslowski, J., and Fox, D.J. (2009). Gaussian 09, Revision A.02 (Wallingford, CT: Gaussian, Inc.).

Gasteiger, J., and Marsili, M. (1980). Interactive partial equalization of orbital electronegativity - A rapid access to atomic charges. Tetrahedron **36:** 3219-3228.

Gibeaut, D.M., Hulett, J., Cramer, G.R., and Seemann, J.R. (1997). Maximal biomass of *Arabidopsis thaliana* using a simple, low-maintenance hydroponic method and favorable environmental conditions. Plant Physiol. **115:** 317-319.

Gordon, J.C., Myers, J.B., Folta, T., Shoja, V., Heath, L.S., and Onufriev, A. (2005). H++: a server for estimating pK(a)s and adding missing hydrogens to macromolecules. Nucleic Acids Res. **33:** W368-W371.

Hansen, B.G., Kerwin, R.E., Ober, J.A., Lambrix, V.M., Mitchell-Olds, T., Gershenzon, J., Halkier, B.A., and Kliebenstein, D.J. (2008). A novel 2-oxoacid-dependent dioxygenase involved in the formation of the goiterogenic 2-hydroxybut-3-enyl glucosinolate and generalist insect resistance in *Arabidopsis*. Plant Physiol. **148:** 2096-2108.

Harris, R., Olson, A.J., and Goodsell, D.S. (2008). Automated prediction of ligand-binding sites in proteins. Proteins **70:** 1506-1517.

Irwin, J.J., Sterling, T., Mysinger, M.M., Bolstad, E.S., and Coleman, R.G. (2012). ZINC: A Free Tool to Discover Chemistry for Biology. J. Chem. Inf. Model. **52:** 1757-1768.

Lee, S., Badieyan, S., Bevan, D.R., Herde, M., Gatz, C., and Tholl, D. (2010). Herbivore-induced and floral homoterpene volatiles are biosynthesized by a single P450 enzyme (CYP82G1) in *Arabidopsis*. Proc. Natl. Acad. Sci. USA **107,** 21205-21210.

Marti-Renom, M.A., Stuart, A.C., Fiser, A., Sanchez, R., Melo, F., and Sali, A. (2000). Comparative protein structure modeling of genes and genomes. Annu. Rev. Biophys. Biomol. Struct. **29:** 291-325.

Melo, F., and Sali, A. (2007). Fold assessment for comparative protein structure modeling. Protein Sci. **16:** 2412-2426.

Melo F, D.D., Depiereux E, Feytmans E. (1997). ANOLEA: a www server to assess protein structures. Proc. Int. Conf. Intell. Syst. Mol. Biol. **5,** 187-190.

Morris, A.L., Macarthur, M.W., Hutchinson, E.G., and Thornton, J.M. (1992). Stereochemical quality of protein-structure coordinates. Proteins **12,** 345-364.

Morris, G.M., Goodsell, D.S., Halliday, R.S., Huey, R., Hart, W.E., Belew, R.K., and Olson, A.J. (1998). Automated docking using a Lamarckian genetic algorithm and an empirical binding free energy function. J. Comput. Chem. **19:** 1639-1662.

Morris, G.M., Huey, R., Lindstrom, W., Sanner, M.F., Belew, R.K., Goodsell, D.S., and Olson, A.J. (2009). AutoDock4 and AutoDockTools4: Automated docking with selective receptor flexibility. J. Comput. Chem. **30:** 2785-2791.

Shen, M.Y., and Sali, A. (2006). Statistical potential for assessment and prediction of protein structures. Protein Sci. **15:** 2507-2524.

Trott, O., and Olson, A.J. (2010). AutoDock Vina: improving the speed and accuracy of docking with a new scoring function, efficient optimization, and multithreading. J. Comput. Chem. **31:** 455-461.

Zimmermann, P., Hirsch-Hoffmann, M., Hennig, L., and Gruissem, W. (2004). GENEVESTIGATOR. *Arabidopsis* microarray database and analysis toolbox. Plant Physiol. **136:** 2621-2632.